Prepared for publication as an Article in the ACS Sensors

Electrokinetic Enrichment and Label-Free Electrochemical Detection of Nucleic Acids by

Conduction of Ions Along the Surface of Bioconjugated Beads

Beatrise Berzina, †, a Umesha Peramune, †, a Sungu Kim, a, b Kumar Saurabh, a, b Echo L. Claus, a

Madison E. Strait, a Baskar Ganapathysubramanian, a,b Robbyn K. Ananda*

^aThe Department of Chemistry, Iowa State University, 2415 Osborn Drive, 1605 Gilman Hall,

Ames, Iowa 50011-1021, United States.

^bThe Department of Mechanical Engineering, Iowa State University, 2043 Black Engineering,

2529 Union Drive, Ames, Iowa 50011-2030, United States.

†These authors contributed equally.

*To whom correspondence should be addressed

E-mail: <u>rkanand@iastate.edu</u>

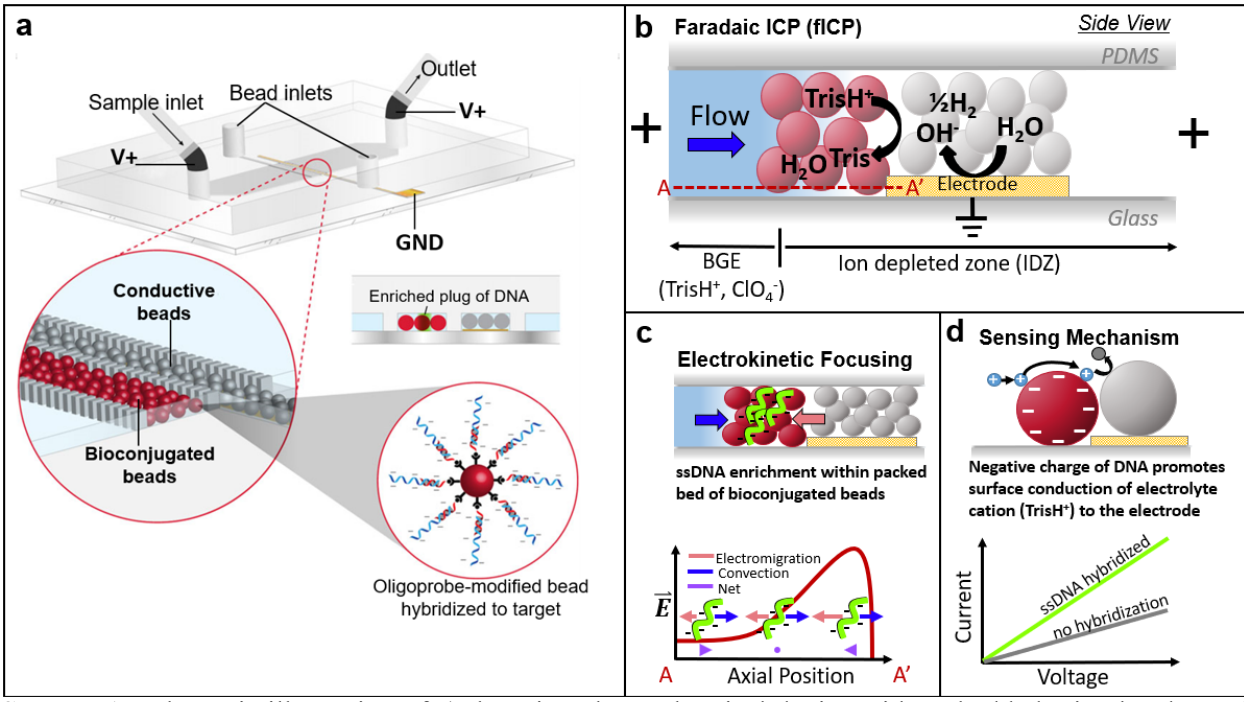
Submitted: November 12, 2022

Abstract

In this paper, we report a method to integrate electrokinetic pre-enrichment of nucleic acids within a bed of probe-modified microbeads with their label-free electrochemical detection. In this detection scheme, hybridization of locally enriched target nucleic acids to the beads modulates the conduction of ions along the bead surfaces. This is a fundamental advancement in that this mechanism is similar to that observed in nanopore sensors, yet occurs in a bed of microbeads with microscale interstices. In application, this approach has several distinct advantages. First, electrokinetic enrichment requires only a simple DC power supply, and in combination with non-optical detection, makes this method amenable to point-of-care application. Second, the sensor is easy to fabricate, comprised of a packed bed of commercially-available microbeads, which can be readily modified with a wide range of probe types, thereby making this a versatile platform. Finally, the sensor is highly sensitive (picomolar) despite the modest 100-fold pre-enrichment we employ here by faradaic ion concentration polarization (fICP). Further gains are anticipated under conditions for fICP focusing that are known to yield higher enrichment factors (up to 100,000-fold enrichment). Here, we demonstrate detection of 3.7 pM singlestranded DNA complementary to the bead-bound oligoprobe, following a 30-min single step of enrichment and hybridization. Our results indicate that a shift in the slope of a current-voltage curve (CVC) occurs upon hybridization, and that this shift is proportional to the logarithm of the concentration of target DNA. Finally, we investigate the proposed mechanism of sensing by developing a numerical simulation that shows an increase in ion flux through the bed of insulating beads given changes in surface charge and zeta potential consistent with our experimental conditions.

Key Words: Electrochemical biosensors, Ion concentration polarization, Nucleic acid diagnostics, Electrokinetic focusing, Analyte preconcentration.

Sensors that leverage the influence of a biorecognition event on charge transport are among the most sensitive because they translate localized binding into a change in a system-scale property. Two premier examples are field effect transistors, in which charged molecules bound to a semiconducting gate modulate the density of states available for electron conduction between the source and drain, and sensors based on nanopores, in which ion conduction along surfaces dominates over bulk transport, thereby amplifying the role of charged surface sites. These features have been leveraged for highly sensitive detection and quantification of biomolecules. Peccently, sensors employing solid-liquid interface capacitance, that rely on surface charge and electric double layer (EDL) thickness change, have emerged. However, fabrication and custom functionalization of these sensors is not trivial, and their integration with protocols that pre-enrich



Scheme 1. Schematic illustration of a) the microelectrochemical device with embedded microbeads used in this study; b) the mechanism of faradaic ICP (fICP) that proceeds via base neutralization of buffer ions comprising the BGE; c) electrokinetic focusing of ssDNA within the packed bed of bioconjugated beads, and d) charge-based sensing mechanism.

target species and facilitate their transport to the biorecognition site is an active area of research. Therefore, there is a need for methods to enrich biomolecules at a binding site and then detect them electrically using a simple and versatile device architecture. We seek to accomplish this goal using ion concentration polarization (ICP) to facilitate electrokinetic focusing of target biomolecules within a bed of probe-conjugated microbeads, where these analytes are then detected based on their modulation of the conduction of electrolyte ions along the bead surfaces.

ICP is the localized enrichment and depletion of background electrolyte (BGE) ions. Depletion of BGE ions can proceed via selective charge transport through a microstructure, such as ion selective membrane or nanochannel, called ICP, or via faradaic (charge transfer) reactions that occur at an electrode, called fICP, under an applied voltage.^{8–11} Scheme 1b illustrates the fICP mechanism via neutralization of buffer ions comprising the BGE in a microfluidic channel with a 3D electrode used in this study. Here, at the 3D electrode, water is reduced to generate OH⁻ ions. Further, an uncharged species (tris(hydroxymethyl)aminomethane, (Tris)) is formed by OHaccepting a proton from the BGE cation (TrisH⁺). The removal of ions of the BGE results in a local decrease in ionic strength and creation of an ion depleted zone (IDZ). The electric field strength within the IDZ is ohmically enhanced, and an extended electric field gradient forms along the IDZ boundary. This gradient can accomplish electrokinetic focusing of charged species in the presence of fluid flow that opposes their electromigration (Scheme 1c) and has been employed extensively for analyte preconcentration, 12-18 water desalination, 9,19 removal of excess fluid from blood plasma,²⁰ separation of particles,²¹ and paper and droplet-based microextraction^{22,23} among other applications. Despite the success of these methods, some aspects of ICP-based enrichment, such as fluidic instability within the IDZ, and integration with downstream analysis, are active areas of research.

Electrokinetic enrichment of biomolecules has been shown previously to increase the sensitivity of bead-based immunoassays. Wang et al. reported an approximate 500-fold increase in the sensitivity of R-phycoerythrin protein detection following 30 min of preconcentration followed by a 30-min binding step to antibody-modified particles. ¹² In related work, Park and coworkers developed a platform combining dielectrophoretic capture of freely suspended biotin-conjugated beads with an ICP-based preconcentration step. This approach increased the sensitivity for detection of avidin at biotin-conjugated particles by 3-fold and opened a route to control bead positioning for localized sensor development. ²⁴ Most recently, Lu et al. reported 162-fold enhanced sensitivity for fluorescently-tagged inflammatory cytokines enriched within a bed of microbeads using a silicon nanogap preconcentrator, which was able to achieve 1000-fold enrichment in 10 min. ²⁵ These results demonstrate that ICP-based preconcentration can enhance the speed and sensitivity of immunoassays, which is advantageous for POC applications. Nevertheless, these assays are limited in scope because they require the analyte to be fluorescent or to be tagged with a fluorescent label.

To address this challenge, Ouyang et al. developed a nanofluidic biosensor (nanofluidic crystal) that used ICP for dual purpose – to decrease the background ion concentration of complex fluids enabling stable electrical detection of proteins and target DNA in urine and serum, and for target preconcentration, improving the LOD of targets from 10-100 nM to 10-100 pM.²⁶ This approach requires packing of submicron beads and target enrichment occurs outside of the packed bed. Senapati et al. developed a label-free non-optical sensor, which employs ICP itself as a reporting mechanism.²⁷ Ion selective structures exhibit distinct non-linear current-voltage curves (CVCs). These authors showed that binding of nucleic acids on the surface of an ion permselective membrane produces a change in ionic current owing to a change in the magnitude of fixed charge

within the IDZ. These processes, in turn, cause a significant shift in the onset potential of characteristic regimes observed in the CVC. This sensor was operated by simply incubating the sample with the membrane for a period of 15 min prior to reading the CVC – there was no electrokinetic preconcentration step. This procedure resulted in a detection limit in the range of 10-100 nM for a 27 bp sequence for a 3.5 mm² and 1 pM for a 1 mm² sensor. Yin and coworkers advanced this approach further, demonstrating sensitive and selective detection of four dengue virus serotypes following RNA extraction from blood plasma and amplification by reverse transcriptase polymerase chain reaction (RT-PCR).²⁸ It is notable that there was still no electrokinetic pre-enrichment step. The LOD for the combination of RT-PCR and the sensor was 100 copies of viral RNA per 1 mL of plasma. In a similar work by Slouka and co-workers, ICPassisted preconcentration was integrated with ICP-assisted sensing to selectively detect a microRNA cancer biomarker (miRNA146a).²⁹ These authors used a cation exchange membrane to preconcentrate the target by ICP and an anion exchange membrane to detect the target using CVC characteristics. The same concept of ICP-mediated preconcentration and sensing was used by Ramshani et al. to quantify both free microRNA and extracellular vesicles containing microRNA in plasma.³⁰ They were able to achieve a detection limit of 1 pM using this method. The key point is that these detection limits are competitive with fluorescence-based methods but require only simple electrical equipment.

Recently, we developed a platform that utilizes packed beds of microbeads to stabilize the focused analyte plug by decreasing the degree of unwanted mixing.³¹ The method employed in the reported device forms an IDZ through faradaic reactions that neutralize electrolyte cations. This faradaic ICP (fICP) was accomplished at a 3D electrode comprising Ag-coated glass microspheres overlying a Au thin film microband. This extension of the electrode out-of-plane of the substrate

allowed the IDZ to be formed over a larger channel cross section, thereby increasing the throughput for sweeping a sample volume. A secondary bead bed composed of polystyrene carboxylate microbeads (PSC) was positioned just upstream of the 3D electrode such that the plug of analyte was focused within the PSC bead bed.³¹ The location of the focused band of analyte within the secondary bead bed provides an opportunity to interface concentration enrichment with a bead-based assay. Therefore, we shifted our attention to the development of a non-optical approach to sense target DNA following hybridization to oligoprobe-modified beads. Importantly, in our device, the hybridization event occurs on the surface of these secondary beads – not that of the electrode or a membrane.

Our previous work showed that the secondary beads play a key role in surface conduction of ions to the electrode, and for that reason, we anticipated that a change in the magnitude of bound surface charge on the bead surface would likewise lead to a shift in the CVC. Therefore, we evaluated the ability of the CVCs in our out-of-plane fICP platform to serve as a non-optical sensing mechanism for hybridization of single-stranded DNA (ssDNA). To explore this possibility, we employed streptavidin-coated microspheres (15-µm diameter) modified with a biotinylated oligonucleotide probe. **Scheme 1** illustrates a 3D Ag/Au electrode sensor with a secondary bead bed composed of probe-modified beads for *in situ* quantification of enriched nucleic acids based on electrical (non-optical) detection.

Here, we demonstrate that hybridization of ssDNA (200-mer) to the oligoprobe-modified beads yields a positive shift in the CVC (increased conductivity), that this signal is specific to the target, and that the magnitude of this shift is proportional to the logarithm of ssDNA concentration. This signal is enhanced by fICP focusing of the ssDNA within the packed bed of probe-modified beads for 30 min prior to sensing. The signal is enhanced in a time-dependent manner, with

diminishing returns at long focusing times since the concentration within the enriched plug increases linearly while signal depends on concentration logarithmically. A key finding is that ion conduction along the surface of these beads is the dominant contributor to current through the bead bed, and therefore, hybridization of a target nucleic acid (a polyanion) to the bead surface leads to a shift in the slope of the CVC. This mechanism is supported by the results of numerical simulations, which quantify ion current to the 3D electrode as a function of the zeta potential, over the relevant range, at the surface of the bioconjugated microbeads. These findings are significant for several reasons. First, in the reported sensing mechanism a binding event modulates conduction of charge carriers despite bead diameters and interstitial spaces being on the microscale. Second, this same device architecture readily supports electrokinetic enrichment, and the two are integrated here. Third, in terms of application, this bead-bed sensor is more straightforward to fabricate (as no membrane modifications or DRIE, RIE etching is required to fabricate nanofeatures to achieve selective ion depletion and/or sensing) and customize than other sensors (all materials are commercially available) in this class and shares the advantage of being non-optical, label-free, and operational at low voltages, rendering it relevant to point-of-need sensing. We were able to achieve a sensitivity of 0.168 µA/log[target] and limit of detection of 3.7 pM using this sensing mechanism, which is comparable to other electrochemical DNA biosensors.³² Note that most of the electrochemical nucleic acid sensors with zM-fM detection limits utilize more complex schemes such as molecularly imprinted polymers, nanostructured electrodes, labeled probes, redox labels, and enzymatic amplification.³³

Experimental Methods

Chemicals. The charged fluorophore, BODIPY²⁻ (4,4-fluoro-1,3,5,7,8-pentamethyl-4-bora-3a,4a-diaza-S-indacene-2,6-disulfonic acid, disodium salt) was obtained from Invitrogen (Carlsbad, CA). All other solutions were prepared using reagent grade chemicals (Fisher Scientific, Waltham, MA) and diluted with double deionized water (18.2 MΩ·cm, Sartorius Arium Pro, Göttingen, Germany) to desired concentration. Poly(dimethylsiloxane) (Sylgard 184 elastomer kit, Dow Corning Corp., Midland, MI) was used for device fabrication. Polystyrene carboxylate beads (diameter, $d = 20 \mu m$) were purchased from Polysciences Inc. (Warrington, PA). Streptavidin coated microspheres ($d = 15 \mu m$, 1% w/v, binding capacity = 0.032 μg biotin-FITC/mg) were purchased from Bangs Laboratories Inc. (Fishers, IN) Conductive silver-coated hollow glass microspheres (d = 10-20 μm, 0.67 g/cc) were purchased from Cospheric (Santa Barbara, CA). Aucoated glass slides with a Cr adhesion layer (1" x 3" x 0.40"; 50 Å Cr, 1,000 Å Au) were purchased from Evaporated Metal Films (Ithaca, NY) and were used for fabrication of patterned thin film electrodes.

Fluorescence imaging and data processing. All fluorescence measurements were obtained using an Eclipse Ti-S inverted fluorescence microscope (Nikon Industries, New York, NY) equipped with a digital camera (Orca Flash 4.0, Hamamatsu Corp., Bridgewater, NJ). All images were processed using NIS-Elements 4.6 software (Nikon). Fluorescence intensities used for calculation of enrichment factor (EF) were background subtracted and processed using NIS-Elements 4.6 software.

Device design and fabrication. The microfluidic devices were fabricated using standard photolithographic processes.³⁴ Channel molds were patterned using negative photoresist (SU-8 2050, Microchem Corp., Westborough, MD) coated on a Si substrate followed by casting with PDMS. **Scheme 1** depicts the device design. The main channel was 40 μm tall, 11.0 mm long, and 1.48 mm wide. The length of the primary bead bed (along the channel) was 300 μm, and there were 10 μm gaps between the posts (20 μm wide) used to retain the beads. Auxiliary channels used for packing the bead beds were 200 μm wide and 2.5 mm long. A 1.0-mm diameter biopsy punch was used to create the inlet and outlet reservoirs of the main channel, and the inlet of the auxiliary channels for bead bed packing.

Au electrodes were microfabricated on glass slides using a previously published method.³⁵ The patterned Au electrode width was 200 µm and it was centered at the midpoint of the main channel, underneath the 3D conductive bead bed. This electrode was sufficiently long to extend out from under the PDMS monolith to make contact to a wire lead. The PDMS layer and glass slide with patterned Au film were treated in an air plasma (PDC-001, Harrick Plasma, Ithaca, NY) for 60 s and then placed in contact to bond. To enhance the bond strength, the device was incubated at 65°C for at least 18 h.

A suspension of the conductive Ag-coated beads in DDI (5.0 μ L, w/v = 22 mg mL⁻¹) was flowed into the primary bead bed by pipetting it into the inlet. The bead inlet was then sealed by adding a drop (approx. 40 μ L) of uncured PDMS. Further, oligoprobe-modified microbeads were packed into the secondary bead bed, and the bead-inlet was sealed using PDMS. It is very important that this PDMS was cured at room temperature overnight to prevent degradation of the modified beads. The driving electrodes comprised 1.0 mm O.D. stainless steel tubing that connected the inlet and outlet of each device to PTFE tubing.

Electrokinetically enhanced assays for single-stranded nucleic acids at a probe-modified bead bed. The sequences of oligonucleotides used in this study (including a 200-mer ssDNA target, 24-mer biotinylated matched probe, a 24-mer biotinylated partially mismatched probe, and a 20-mer biotinylated mismatched probe) are provided in the *Supporting Information*. All oligonucleotides were purchased from Integrated DNA Technologies (Coralville, IA). **Scheme S1** illustrates the configuration and the oligonucleotide hybridization scheme utilized in the assay.

Attachment of biotinylated oligonucleotide to streptavidin-coated microspheres. Biotinylated oligonucleotide (probe) was bound to the streptavidin-modified beads following a published procedure.³⁶ First, 100 μL of the bead suspension was rinsed two times with 100 μL of a wash buffer (20.0 mM Tris buffer, pH 7.5, 1.0 M NaCl, 1.0 mM EDTA, and 0.0005% Triton X-100) by centrifuging the beads at 5000 rpm for 3 min, and decanting the supernatant. Second, the beads were resuspended into 20 μL of wash buffer and 11.5 μg of the probe. The beads were incubated at 500 rpm (ThermoMixer C, Eppendorf, Hauppauge, NY) for 20 min at 20 °C. Third, unbound probe was removed by rinsing twice with 100 μL of the wash buffer and one with 100 μL of Tris·HClO₄ buffer (10.0 mM, pH 8.3, with 0.2 mM MnCl₂ added), centrifuging the beads at 5000 rpm for 3 min, and decanting the supernatant. Lastly, these oligo-bound streptavidin microspheres (Probe-SV beads) were re-suspended in 100 μL of Tris·HClO₄ buffer (10.0 mM, pH 8.3, with 0.2 mM MnCl₂ added) and stored at 4°C until use (up to 2 weeks at most).

Electrochemical (non-optical) detection of nucleic acids and assay procedure. To facilitate device filling, devices were evacuated under vacuum for 20 min prior to rinsing with Tris·HClO₄ buffer

(10.0 mM, pH 8.3, with 0.2 mM MnCl₂ added) for 1 h, at 500 nL min⁻¹. Prior to use, devices were conditioned at 3.0 V for 5 min, at 500 nL min⁻¹, and a background fluorescence image was obtained. Further, the flow rate was decreased to 10 nL min⁻¹ for 10 min and a first CVC was obtained. **Scheme S2** shows the device and electronic configuration used for applying the potential bias during enrichment and obtaining the CVCs.

For the assay, first, buffer solution was replaced with the assay solution (10.0 mM Tris·HClO₄, 0.2 mM MnCl₂, 0.1 μ M BODIPY²⁻ and the concentration of ssDNA indicated in each experiment in the *Results and Discussion* subsection). Second, the flow rate was set to 10 nL min⁻¹ for 10 min and a second set of CVCs was obtained. Third, the flow rate was increased to 90 nL min⁻¹, and $V^+ = 7.0$ V applied between the driving electrodes and the wire lead connected to the 3D Ag/Au electrode. Accumulation of the BODIPY²⁻ was monitored by fluorescence microscopy for 30 min after the driving voltage was applied. Fourth, after 30 min of enrichment, the applied voltage was turned off, and the device was rinsed by increasing the flow rate to 500 nL min⁻¹ for 5 min to remove all non-specifically bound species. Last, a third set of CVCs was obtained. To account for the impact of electrokinetic enrichment itself on ionic conductivity, a background current measurement (the first CVC obtained, in Tris·HClO₄ buffer alone) was subtracted from those obtained prior to and after enrichment. The procedure is illustrated in **Scheme S3**.

Results and Discussion

Enrichment of DNA by fICP within a packed bed of microbeads. Towards integration of electrokinetic enrichment and sensing of nucleic acids, we first verified that ssDNA is focused

within the secondary bead bed. Figure 1a is a brightfield micrograph showing the central segment of the microchannel (top view), in which two packed beds of microbeads are defined by three rows of retention pillars. A bed of probe-modified streptavidin microbeads (Probe-SV) is upstream of the 3D electrode defined by Ag-coated glass microbeads overlying a thin film Au microband. Our previous study demonstrated that BODIPY2- is focused within the secondary bead bed (bare polystyrene carboxylate beads) in this device,³¹ and therefore, since ssDNA has a similar electrophoretic mobility to that of BODIPY²⁻, its enrichment within this bead bed was anticipated. The ssDNA focusing was evaluated as follows. First, the microchannel was rinsed and preconditioned as described in the Experimental Methods section. Then, a solution comprising a fluorescently tagged ssDNA secondary probe (0.4 µM) and 20 pM ssDNA target in 20.0 mM Tris·HClO₄ (pH 8.3) was flowed into the inlet at 100 nL min⁻¹. This 24-mer secondary probe was designed to be fully complementary to the ssDNA target and was tagged at the 3' end with 6-Carboxyfluorescein (6-FAM). Finally, $V^+ = 7.0 \text{ V}$ was applied (at t = 0) between the driving electrodes and the wire lead connected to the 3D Ag/Au electrode. Figure 1b-d is a time series of fluorescence micrographs demonstrating the formation of an enriched plug of the fluorescently tagged secondary probe within the probe-modified bead bed at t = 1, 30, and 60 min afterapplication of this voltage bias. Both the projected area and intensity of the fluorescent plug increased, demonstrating enrichment. Figure 1e is a plot of the calculated EF as a function of time. 300-fold enrichment of the fluorescently tagged ssDNA was achieved within 60 min. This result

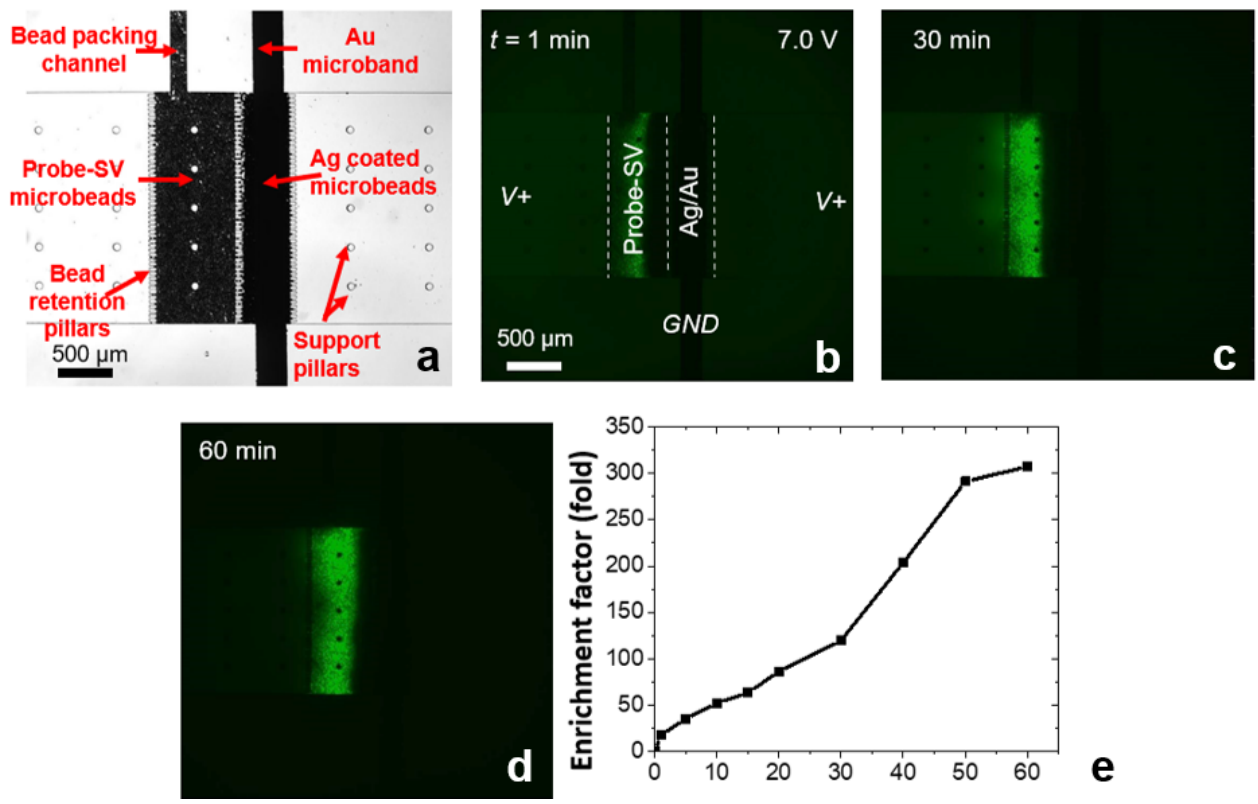


Figure 1. a) Brightfield micrograph of the device (top view) with oligo-bound streptavidin microspheres (Probe-SV) and Ag bead beds located at the center of the microchannel. **b-d)** Time series of fluorescence micrographs showing co-enrichment of the FAM-tagged ssDNA at t = 1-, 30-, and 60-min following initiation of an applied voltage of $V^+ = 7.0 \text{ V}$ to a Probe-SV/Ag/Au device. During experiment, the channel was continuously infused with 0.4 μ M fluorescently tagged ssDNA secondary probe and 20.0 pM ssDNA target in 20.0 mM Tris (pH 8.3) at 100 nL min⁻¹. **e)** Plot showing evolution of enrichment factor over time for the fluorescently tagged ssDNA secondary probe.

is significant because it shows that ssDNA is electrokinetically enriched within the probe-modified bead bed. This occurs under similar flow rate (90 nL min⁻¹) and voltage (7.0 V) previously reported for enrichment of BODIPY²⁻,³¹ which indicates that this dye has an appropriate mobility to estimate the focusing location of ssDNA. These conditions were therefore carried forward to subsequent experiments in the presence of BODIPY²⁻ and absence of the secondary probe.³¹

Label-free sensing of target ssDNA following electrokinetic focusing within a packed bed of probemodified beads. We next tested the hypothesis that the hybridization of target ssDNA to the ProbeSV beads could lead to a change in ionic conductivity in that channel segment. The assay experiment proceeded as described in the *Experimental Methods*.

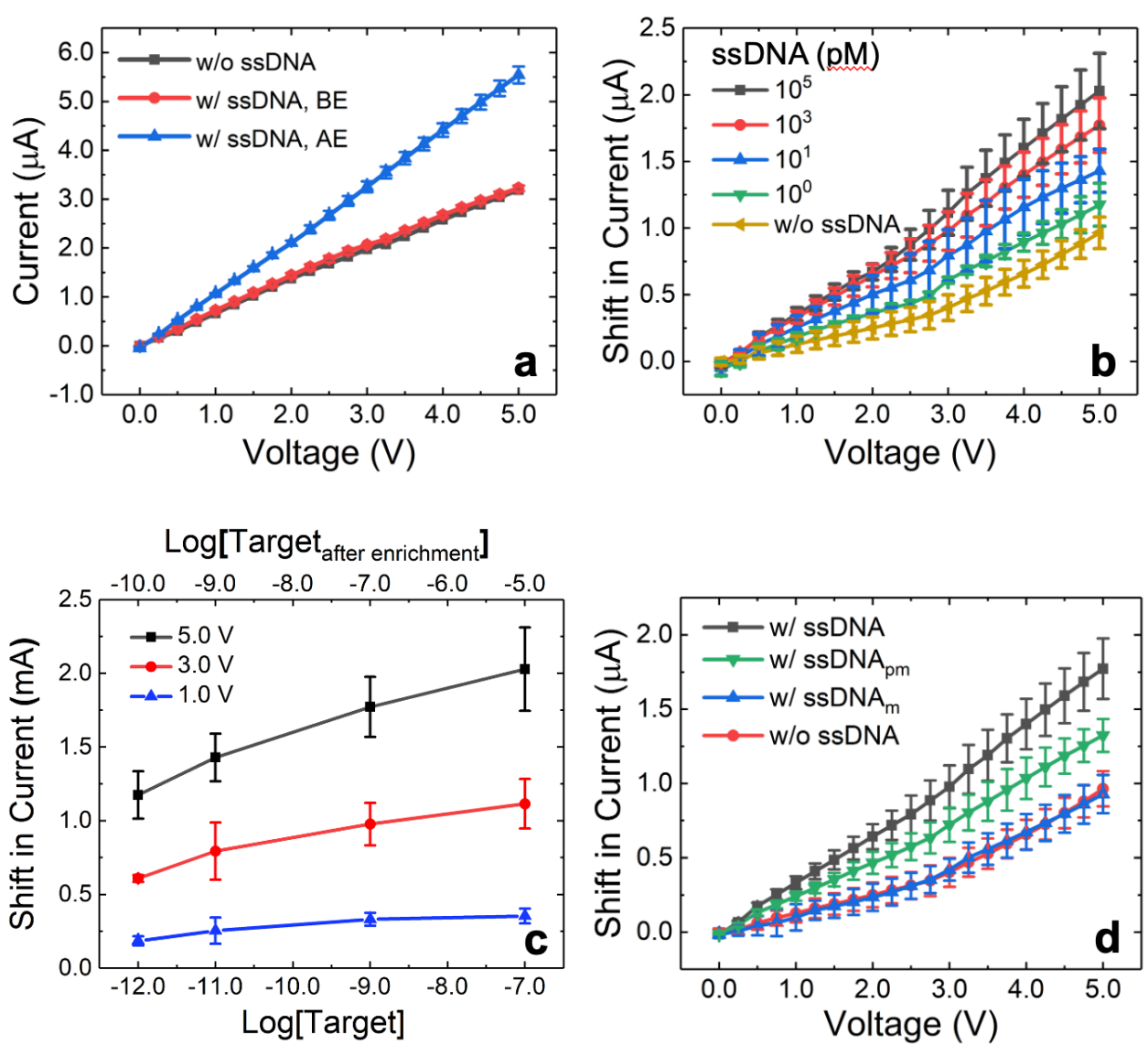


Figure 2. a) Series of CVCs for 1.0 nM target ssDNA in 20.0 mM Tris·HClO₄, pH 8.3 before (BE, red trace) and after (AE, blue trace) enrichment in comparison to a sample where no ssDNA target is added (black trace); **b)** Shift in current as a function of voltage for several ssDNA target concentrations; **c)** Plot of the shift in current as a function of the logarithm of target concentration before enrichment, and as a function of the logarithm of target concentration after enrichment (assuming 100-fold preconcentration) at several distinct voltages (1.0 V, 3.0 V and 5.0 V) extracted from the curves shown in (b); **d)** Shift in current as a function of voltage for ssDNA target (1.0 nM, black trace), partial mismatch (ssDNA_{pm}, green trace, 1.0 nM), complete mismatch (ssDNA_m, blue trace 1.0 nM) in comparison to a sample where no ssDNA is added (red trace), all in 10.0 mM Tris·HClO₄, (pH 8.3, 0.2 mM MnCl₂ added).

Figure 2a shows the CVCs obtained at three time points: 1) prior to introduction of ssDNA target (black trace), 2) following 30 min of exposure to the assay solution (0.1 μ M BODIPY²⁻, 1.0 nM ssDNA, 10.0 mM Tris with 0.2 mM MnCl₂ added) before enrichment (BE, red trace), and 3) after enrichment for 30 min and a rinse (AE, blue trace). After enrichment, a significant shift in the CVC was observed, in which the resistance measured in the ohmic regime is approximately halved (1.76-fold steeper slope). Such a large shift was not observed in the absence of enrichment, which implies that the shift results from electrokinetic enrichment and hybridization of target ssDNA to the bioconjugated microspheres.

We next evaluated whether this signal was caused by the presence of ssDNA (and not by the fICP process alone) by varying its concentration. **Figure 2b** is a plot of the CVC shift (difference in current obtained after enrichment (AE) and the background current, w/o ssDNA) as a function of applied voltage obtained for target ssDNA at several distinct concentrations in the range of 1 to 10⁵ pM. We attribute the slight change in slope around 3.0 V to the onset of OH generation and sequential BGE ion depletion, required for IDZ formation. A key point is that the CVC shift increased linearly with the logarithm of the concentration of the target regardless of voltage (**Figure 2c**). This relationship is characteristic of the specific interaction (binding or hybridization) of a target analyte with a limited number of probe sites and can be modeled by a modified adsorption isotherm.

Therefore, based on this result, we conclude that the signal arises from hybridization of ssDNA to the probe-modified beads. This finding is important because it implies that the signal (shift in current) arises from a change in conductivity within this bead bed. Since current is conducted via ions through this channel segment, we attribute the signal to a change in the density and distribution of nucleic acids (polyanions) that enhances surface conduction of ions (e.g.,

TrisH⁺). This sensing mechanism is similar to that reported for sensors that rely on analyte-driven modulation of ion conduction through nanopores, yet the interstitial spaces between these microbeads is much larger (about 2 μ m). We estimate that the Dukhin number (Du), which describes the relative magnitude of surface conductance (G_{surf}) to bulk conductance (G_{bulk}) of ions, falls within the range of 0.6 to 6 for fully de-hybridized to hybridized probes. This range implies that surface conduction of ions contributes up to 85% of the current through this bead bed. This quantity can be estimated by the following equation.

$$Du = \frac{G_{surf}}{G_{bulk}} = \frac{\sigma}{Fhzc_0} \tag{1}$$

Here, σ is the density of bound surface charges, F is the Faraday constant, h the height of the pore (or interstitial space), z charge number (here, z=1 for a 1:1 electrolyte), and c_0 is the electrolyte concentration. We assumed a surface coverage of 6.3×10^{12} probes/cm² based on the biotin-binding capacity provided by the manufacturer of the SV-modified beads.

Based on the calibration curve obtained at 5.0 V (**Figure 2c**), we determined the limit of detection (LOD) of this label-free, non-optical fICP sensor to be 3.7 pM. This LOD was calculated as the concentration at which the shift in current is equal to $I_{blank} + 3\sigma$ where I_{blank} is the average shift in current at 5.0 V for seven blanks (without ssDNA) and σ is the standard deviation. The calculated sensitivity is 0.168 μ A/log[target]. A key point is that this excellent performance was obtained with modest enrichment (10^2 -fold, while 10^5 -fold has been reported for fICP) and without optimization of the sensor – only one set of CVC conditions, bead and device dimensions, probe type, and electrolyte composition was tested. Further improvement in LOD is anticipated following a parametric study. We expect that the sensor should reach saturation at higher concentrations. However, within the relevant concentration range, we did not observe saturation.

To test the selectivity of this sensor towards target ssDNA, we repeated this fICP-enhanced assay in the presence of 1.0 nM matched (ssDNA), mismatched (ssDNA_m), or partially mismatched (ssDNA_{pm}) oligonucleotides (sequences can be found in the SI). Figure 2d is a plot of the CVC shift for each of these three ssDNA sequences. Notably, no significant shift in current was observed for fully mismatched ssDNA (Figure 2d, blue trace) from that obtained for buffer solution alone (Figure 2d, red trace). This finding is important because it confirms that the observed signal arises from hybridization (not just the presence) of ssDNA on the probe-modified beads. We observed a diminished shift in current (Figure 2d green trace) with partially mismatched ssDNA (14 of 24 bases matched according to EMBOSS Water pairwise sequence alignment software) in comparison to that of our target (Figure 2d, black trace). This signal for 1.0 nM partial mismatch corresponds to the signal expected for 5.0 pM matched DNA (200-fold selectivity). Note that this probe type is not expected to yield high selectivity. We estimate that this sensor is operating in a regime where the target DNA is depleted by hybridization due to the high affinity of the 24-mer probe and the high concentration of surface sites.³⁷ Under this condition, the sensor is expected to be quantitative yet should exhibit poor specificity. Better selectivity is expected from a shorter probe, especially one comprising a stem-loop configuration or certain xenonucleic acids (XNAs) such as peptide nucleic acids (PNA).

Quantification of the impact of electrokinetic enrichment on DNA sensing. To better understand the role of fICP focusing in this microfluidic bead-based assay, we performed a series of control experiments, in which the shift in current was evaluated as a function of the duration of enrichment.

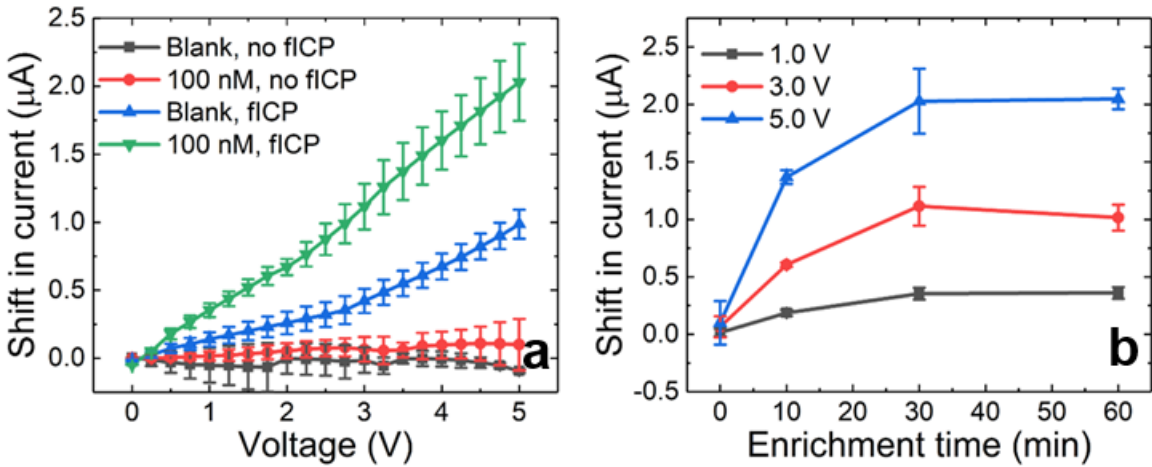


Figure 3. a) Shift in CVCs obtained for 30 min incubation in the absence and presence of fICP-driven enrichment for each target DNA and a blank. **b)** Plot of the shift in current observed in CVCs obtained following separate experiments with 0, 10, 30, and 60 min of enrichment from target DNA. The shift in current at only selected voltages (1.0, 3.0, and 5.0 V) are shown for clarity. (a and b) The solution comprised 100 nM target ssDNA in 0.1 μ M BODIPY²⁻, 0.2 mM MnCl₂, and 10.0 mM Tris·HClO₄ at pH 8.3. Applied voltage, $V^+ = 7.0$ V. For each condition, n = 3, separate devices.

Figure 3a is a plot of the CVC shifts obtained both for a blank and for 100 nM target under two distinct conditions – with and without enrichment by fICP. The devices were preconditioned (at $V^+ = 3.0 \text{ V}$) as before, and the devices were filled with 100 nM ssDNA target, 0.1 μ M BODIPY²⁻, and 10.0 mM Tris·HClO₄ with 0.2 mM MnCl₂. The samples were analyzed as described for the data in Figure 2a with the exception that during the 30-min incubation of the sample (flowed at 90 nL min⁻¹), the voltage ($V^+ = 7.0 \text{ V}$) was not applied for the two cases labeled "no fICP". This data shows that in the absence of enrichment, the blank (black trace) has a near zero shift in current. This result is remarkable when compared to a significant shift (1.0 μ A at 5.0 V) obtained for a blank subjected to fICP (blue trace), which we attribute to processes independent of DNA and directly linked to the applied voltage, such as redistribution of BGE ions and changes in the electrode surface. More importantly, the shift in the CVC obtained for 100 nM target DNA (red trace) in the absence of enrichment (no fICP) is not significantly higher than the corresponding blank (black trace), whereas, following enrichment, the signal for 100 nM target (green trace) is

just over 2.0 μ A, which is well separated from the corresponding blank (blue trace). This result indicates that fICP plays a key role in the ability of this device to sense DNA following 30 min incubation.

Our hypothesis is that fICP increases sensitivity by enriching the local concentration of target DNA within the packed bed of bioconjugated beads. Therefore, the sensitivity of this device is expected to depend on the duration of enrichment. To test this hypothesis, we evaluated the shift in CVCs obtained for separate experiments ending after 0, 10, 20, 30, and 60 min of enrichment. Figure 3b shows the shift in current extracted from these CVCs at 1.0, 3.0, and 5.0 V. Notably, this signal increases over time until 30 min, after which it reaches a near constant value. This limiting value is reached despite our previous observation that the concentration of fluorescently tagged DNA triples over the time period between 30 min and 60 min of enrichment (Figure 1e). This result can be understood as arising from the logarithmic dependence of the signal (shift in current) on the concentration of target DNA. Since the surface coverage at equilibrium grows with the logarithm of the target concentration while EF grows linearly, there is a diminishing return on enrichment. Consider that in Figure 1e, the concentration of tagged DNA increased linearly, yielding a 100-fold increase within the first 30 min, but only a 3-fold increase (to a total of EF = 300) within the next 30 min. This linear dependence of EF on enrichment time occurs because the rate of accumulation depends on mass transport of the target DNA to the enriched plug as dictated by the flow rate. This information is important to the design of fICP enhanced assays and indicates that significant gains in signal (versus those obtained here) will be obtained with either much longer enrichment times (e.g., EF predicted to be 1000-fold at 3 h enrichment) or optimization of conditions (dimensions, flow rate, voltage pattern) to achieve more rapid enrichment.

Numerical simulation to investigate the effect of ζ potential on device performance. To understand the observed effect of DNA hybridization on ionic current through the packed bed of microbeads, we numerically investigated the correlation between bead surface charge to ion flux at the electrode by solving the coupled Navier-Stokes and Poisson-Nernst-Planck (NS-PNP) system of equations. The PNP set of equations is used to model charge transport, and fluid motion is represented by a NS system with forcing terms. The forcing terms result from the two-way coupling between the NS and PNP. The non-dimensional forms of the NS-PNP equations are as follows:

Navier-Stokes (NS):
$$\frac{1}{Sc}\frac{d\vec{u}}{dt} + \vec{u} \cdot \nabla \vec{u} = -\nabla p + \nabla^2 \vec{u} - \frac{\kappa}{2\Lambda^2} \rho \nabla \phi$$
 (2)

Poisson (P):
$$-2\Lambda^2 \nabla^2 \phi = \rho \tag{3}$$

Nernst-Planck (NP):
$$\frac{dc_i}{dt} + \vec{u} \cdot \nabla c_i = \nabla \cdot (\nabla c_i + z_i c_i \nabla \phi)$$
 (4)

where \vec{u} , p, ϕ are fluid velocity, pressure, and electric potential. c_i , z_i represents the concentration and valence of species i respectively. κ is electrohydrodynamic coupling constant given by

$$\kappa = \frac{\epsilon}{\eta D} \left(\frac{RT}{F}\right)^2 \tag{5}$$

where ϵ , η , D, R and T are permittivity of fluid, viscosity, average diffusivity, ideal gas constant, and temperature, respectively. ρ is charge density, which is given by:

$$\rho = \sum_{i=1}^{N} z_i c_i \tag{6}$$

The non-dimensional parameters for the governing equations are:

Schmidt number
$$(Sc) = \frac{\eta}{\rho_1 D}$$
 (7)

Debye layer thickness
$$(\Lambda) = \frac{\lambda}{L_c}$$
 (8)

Where λ is the dimensional Debye layer thickness, η is the viscosity of the fluid, ρ_l is the density and D is the diffusivity of charge carriers. L_c denotes the characteristic domain length of the channel, and I_b is the ionic strength of the bulk solution.

$$\lambda = \sqrt{\frac{1}{2} \frac{\epsilon RT}{F^2 I_b}}; I_b = \frac{1}{2} \sum_{i=1}^{N} z_i^2 c_i$$
 (9)

The fully coupled NS-PNP equations were numerically solved using the finite element method (FEM). The details of the numerical methods can be found in our previous method paper.³⁷ Briefly, NS and PNP are solved in a block iterative manner. For the NS equation, the non-linear convection term was linearized. The BDF 2 scheme was used for the temporal discretization and linear basis function was used for spatial discretization. The standard variational multiscale method (VMS) was used for solving the NS equation.³⁸ For the PNP equation, a SUPG (streamline upwind Petrov-Galerkin) style stabilizer was adopted for the convection and electromigration terms. In addition, we utilize an incomplete octree based adaptive mesh generation technique that enables massive parallelization along with the ability to carve out complex objects.³⁹

Zeta potential, denoted by ζ , describes the potential difference between the bulk, electroneutral solution and the potential at the wall. Since, the bulk potential is not known *a priori*, but is a time dependent variation, the imposition of the zeta potential needs careful attention. In this work, we convert zeta potential to an equivalent surface charge density q'', using Graham's equation

$$q'' = \frac{\epsilon \zeta}{\lambda} \left(\frac{2}{z\zeta^*} \sinh\left(\frac{z\zeta^*}{2}\right) \right) \tag{10}$$

where ζ^* is the zeta potential normalized by the thermal voltage.⁴⁰ The equivalent surface charge density is then imposed as a Neumann boundary condition on the surface of PS beads.

We deployed the framework to simulate the effect of zeta potential variation on the flux of ions to the 3D electrode. The validation result of the framework is published in the previous literature.³⁷ To maintain a balance between the computational cost and relevant physics, the non-dimensional Λ was restricted to $O(10^{-3})$. Previous reports have demonstrated the efficacy of this Λ to capture all the relevant physics.⁴¹ Additional detail on the computational domain and boundary condition is provided in SI.

Figure 4 shows the current dependence on the Zeta potential. The current reported is the net sum of the ion flux at the surface of the Ag and Au electrodes. The range of zeta potential for simulation was chosen in accordance with the experimental range of [-27, -30] mV (see **Table S1** in the *SI* for experimentally measured zeta potentials). We observe a linear variation of current with respect to the zeta potential in this range. The current shift is measured with respect to zeta potential of 0 mV. Note that while the fraction of occupied probe sites, surface charge, zeta potential, and the shift in current are linearly related to each other over the investigated range, they depend on the logarithm of target DNA concentration.

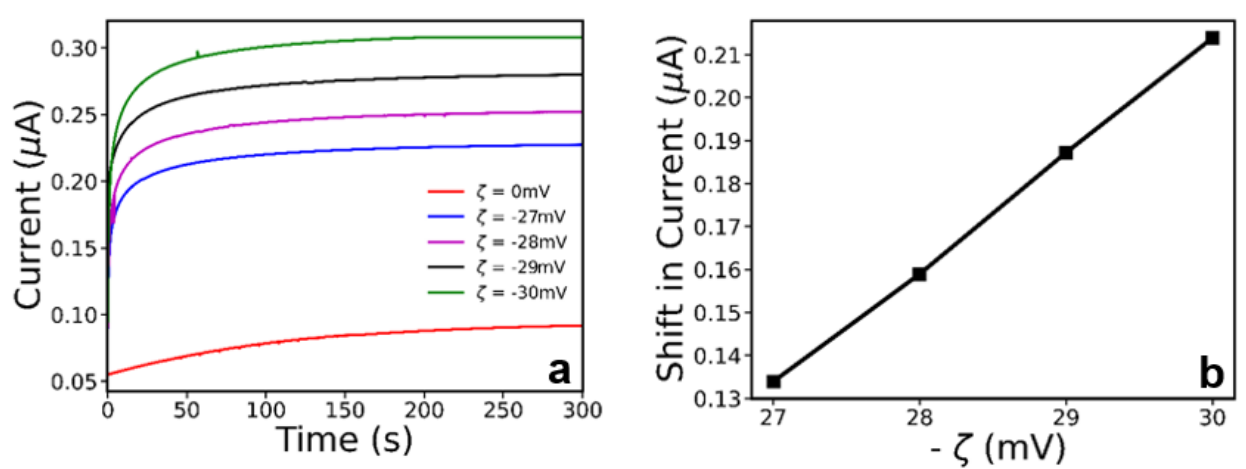


Figure 4. a) Simulated current at the 3D electrode as a function of time after voltage application plotted for several distinct zeta potentials. b) Shift in current at t = 300 s as a function of zeta potential.

Figure 5 is a set of surface plots of the non-dimensional charge density normalized by the bulk concentration at 0 mV and -30 mV zeta potential and taken along xy slices at 10 μ m and 30 μ m above the channel floor. We see a significant difference in the charge density, especially near the bioconjugated beads, where the concentration of cations is higher than that of anions. Similar variation is observed near the 3D (Ag and Au) electrode, with charge on the bioconjugated beads resulting in an increased value of charge density at the electrode surface. This result supports the proposed sensing mechanism of hybridization of target DNA leading to a change in surface charge on the beads, and ultimately, increased ion conduction through the packed bed.

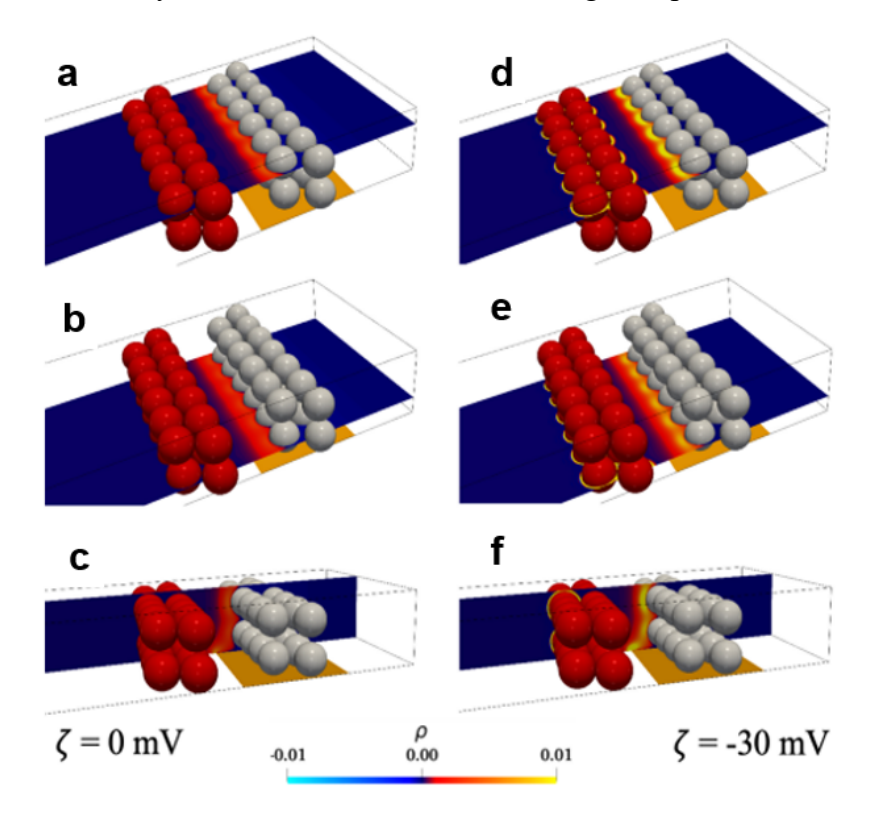


Figure 5. Variation of charge density $(\rho = \frac{c_1 - c_2}{c_0})$ at two distinct values of the zeta potential (ζ) at the bioconjugated bead surface. A distinct zone of positive charge density $(c_1 > c_2)$ is observed near the PS beads for non-zero ζ . Surface plots along the xy-planes located at z = 10 and $30 \mu m$ above the channel floor and along the xz-plane at the channel midline are shown for (a-c) $\zeta = 0$ mV and (d-f) $\zeta = -30$ mV.

Conclusion

We have demonstrated simultaneous preconcentration and in situ quantification of electrokinetically enriched nucleic acids by non-optical (electrochemical) label-free detection, making this approach advantageous for point-of-care (POC) testing. Hybridization of target DNA on the bioconjugated bead bed enhances the surface conduction of charge carriers towards the surface of the sensor, which leads to a positive shift in the slope of a current-voltage curve. This shift varies linearly with the logarithm of the concentration of target DNA. Under the reported conditions, the sensor was able to achieve a limit of detection of 3.7 pM, and a sensitivity of 0.168 μA/log[target]. We anticipate that this approach will allow for high-throughput enrichment and *in situ* electrochemical detection of a wide range of biologically and clinically relevant analytes by simply selecting the appropriate bioconjugated beads. This sensing mechanism is broadly applicable to biorecognition events that result in a change in zeta potential (*SI*, **Table S1**) of the beads and is amenable to multiplexing to increase specificity. A key point is that this method offers 'plug-and-play' enrichment and detection of unlabeled biomolecules because it is compatible with commercially available conjugated beads.

Declaration of competing interest

Authors declare no competing interest.

Acknowledgements

This work was supported by an NSF CAREER grant awarded by the Chemistry Directorate Chemical Measurement and Imaging Program under award number 1849109.

Supplementary data

Supplementary data associated with this article can be found in the online version. Supplementary data includes sequences of each oligonucleotide employed in this study, a diagram of electrical connections to the device under study, a summarized procedure for enrichment and assay, methods and results of the measurement of zeta potential of the bioconjugated beads, current-time curves obtained during pre-conditioning and enrichment steps, a CVC obtained for 100 fM target ssDNA, and CVCs obtained over a larger voltage range (to 15 V).

References

- (1) Macchia, E.; Manoli, K.; di Franco, C.; Picca, R. A.; Österbacka, R.; Palazzo, G.; Torricelli, F.; Scamarcio, G.; Torsi, L. Organic Field-Effect Transistor Platform for Label-Free, Single-Molecule Detection of Genomic Biomarkers. ACS Sens 2020, 5 (6), 1822–1830. https://doi.org/10.1021/acssensors.0c00694.
- (2) Thakur, A. K.; Movileanu, L. Single-Molecule Protein Detection in a Biofluid Using a Quantitative Nanopore Sensor. *ACS Sens* **2019**, *4* (9), 2320–2326. https://doi.org/10.1021/acssensors.9b00848.
- (3) Lee, K.; Lee, H.; Lee, S. H.; Kim, H. M.; Kim, K. B.; Kim, S. J. Enhancing the Sensitivity of DNA Detection by Structurally Modified Solid-State Nanopore. *Nanoscale* **2017**, *9* (45), 18012–18021. https://doi.org/10.1039/c7nr05840c.
- (4) Ying, Y. L.; Long, Y. T. Nanopore-Based Single-Biomolecule Interfaces: From Information to Knowledge. *J Am Chem Soc* **2019**, *141* (40), 15720–15729. https://doi.org/10.1021/jacs.8b11970.
- (5) Sadighbayan, D.; Hasanzadeh, M.; Ghafar-Zadeh, E. Biosensing Based on Field-Effect Transistors (FET): Recent Progress and Challenges. *TrAC* **2020**. https://doi.org/10.1016/j.trac.2020.116067.
- (6) Qi, H.; Hu, Z.; Yang, Z.; Zhang, J.; Wu, J. J.; Cheng, C.; Wang, C.; Zheng, L. Capacitive Aptasensor Coupled with Microfluidic Enrichment for Real-Time Detection of Trace SARS-CoV-2 Nucleocapsid Protein. *Anal Chem* **2022**, *94* (6), 2812–2819. https://doi.org/10.1021/acs.analchem.1c04296.
- (7) Mahmoodi, S. R.; Xie, P.; Zachs, D. P.; Peterson, E. J.; Graham, R. S.; Kaiser, C. R. W.; Lim, H. H.; Allen, M. G.; Javanmard, M. Single-Step Label-Free Nanowell Immunoassay Accurately Quantifies Serum Stress Hormones within Minutes. *Sci Adv.* **2021**, 7(21). https://www.science.org/doi/10.1126/sciadv.abf4401.
- (8) Berzina, B.; Anand, R. K. Tutorial Review: Enrichment and Separation of Neutral and Charged Species by Ion Concentration Polarization Focusing. *Anal Chim Acta* **2020**, *1128*, 149–173. https://doi.org/10.1016/j.aca.2020.06.021.
- (9) Kim, S. J.; Ko, S. H.; Kang, K. H.; Han, J. Direct Seawater Desalination by Ion Concentration Polarization. *Nat Nanotechnol* **2010**, *5* (4), 297–301. https://doi.org/10.1038/nnano.2010.34.

- (10) Kim, J.; Cho, I.; Lee, H.; Kim, S. J. Ion Concentration Polarization by Bifurcated Current Path. *Sci Rep* **2017**, 7 (1). https://doi.org/10.1038/s41598-017-04646-0.
- (11) Anand, R. K.; Sheridan, E.; Knust, K. N.; Crooks, R. M. Bipolar Electrode Focusing: Faradaic Ion Concentration Polarization. *Anal Chem* **2011**, *83* (6), 2351–2358. https://doi.org/10.1021/ac103302j.
- (12) Wang, Y. C.; Han, J. Pre-Binding Dynamic Range and Sensitivity Enhancement for Immuno-Sensors Using Nanofluidic Preconcentrator. *Lab Chip* **2008**, *8* (3), 392–394. https://doi.org/10.1039/b717220f.
- (13) Li, X.; Luo, L.; Crooks, R. M. Faradaic Ion Concentration Polarization on a Paper Fluidic Platform. *Anal Chem* **2017**, *89* (7), 4294–4300. https://doi.org/10.1021/acs.analchem.7b00365.
- (14) Son, S. Y.; Lee, H.; Kim, S. J. Paper-Based Ion Concentration Polarization Device for Selective Preconcentration of Muc1 and Lamp-2 Genes. *Micro and Nano Systems Letters* **2017**, *5* (1). https://doi.org/10.1186/s40486-017-0042-1.
- (15) Han, S. il; Yoo, Y. K.; Lee, J.; Kim, C.; Lee, K.; Lee, T. H.; Kim, H.; Yoon, D. S.; Hwang, K. S.; Kwak, R.; Lee, J. H. High-Ionic-Strength Pre-Concentration via Ion Concentration Polarization for Blood-Based Biofluids. *Sens Actuators B Chem* 2018, 268. https://doi.org/10.1016/j.snb.2018.04.144.
- (16) Wang, Y. C.; Stevens, A. L.; Han, J. Million-Fold Preconcentration of Proteins and Peptides by Nanofluidic Filter. *Anal Chem* **2005**, *77* (14), 4293–4299. https://doi.org/10.1021/ac050321z.
- (17) Ouyang, W.; Han, J. Universal Amplification-Free Molecular Diagnostics by Billion-Fold Hierarchical Nanofluidic Concentration. *Proc Natl Acad Sci U S A* **2019**, *116* (33), 16240–16249. https://doi.org/10.1073/pnas.1904513116.
- (18) Wei, X.; Panindre, P.; Zhang, Q.; Song, Y. A. Increasing the Detection Sensitivity for DNA-Morpholino Hybridization in Sub-Nanomolar Regime by Enhancing the Surface Ion Conductance of PEDOT:PSS Membrane in a Microchannel. *ACS Sens* **2016**, *1* (7), 862–865. https://doi.org/10.1021/acssensors.6b00169.
- (19) Knust, K. N.; Hlushkou, D.; Anand, R. K.; Tallarek, U.; Crooks, R. M. Electrochemically Mediated Seawater Desalination. *Angewandte Chemie International Edition* **2013**, *52* (31), 8107–8110. https://doi.org/10.1002/anie.201302577.

- (20) Berzina, B.; Anand, R. K. An Electrokinetic Separation Route to Source Dialysate from Excess Fluid in Blood. *Anal Chem* **2018**, *90* (6), 3720–3726. https://doi.org/10.1021/acs.analchem.7b02584.
- (21) Davies, C. D.; Crooks, R. M. Focusing, Sorting, and Separating Microplastics by Serial Faradaic Ion Concentration Polarization. *Chem Sci* **2020**, *11* (21), 5547–5558. https://doi.org/10.1039/d0sc01931c.
- (22) Kim, S.; Ganapathysubramanian, B.; Anand, R. K. Concentration Enrichment, Separation, and Cation Exchange in Nanoliter-Scale Water-in-Oil Droplets. *J Am Chem Soc* **2020**, *142* (6), 3196–3204. https://doi.org/10.1021/jacs.9b13268.
- (23) Krishnamurthy, A.; Anand, R. K. Recent Advances in Microscale Extraction Driven by Ion Concentration Polarization. *TrAC* **2022**, 148. https://doi.org/10.1016/j.trac.2022.116537.
- (24) Park, S.; Yossifon, G. Combining Dielectrophoresis and Concentration Polarization-Based Preconcentration to Enhance Bead-Based Immunoassay Sensitivity. *Nanoscale* **2019**, *11* (19), 9436–9443. https://doi.org/10.1039/c9nr02506e.
- (25) Lu, B.; Maharbiz, M. M. Ion Concentration Polarization (ICP) of Proteins at Silicon Micropillar Nanogaps. *PLoS One* **2019**, *14* (11). https://doi.org/10.1371/journal.pone.0223732.
- Ouyang, W.; Han, J.; Wang, W. Enabling Electrical Biomolecular Detection in High Ionic Concentrations and Enhancement of the Detection Limit Thereof by Coupling a Nanofluidic Crystal with Reconfigurable Ion Concentration Polarization. *Lab Chip* **2017**, *17* (22), 3772–3784. https://doi.org/10.1039/c7lc00722a.
- (27) Senapati, S.; Slouka, Z.; Shah, S. S.; Behura, S. K.; Shi, Z.; Stack, M. S.; Severson, D. W.; Chang, H. C. An Ion-Exchange Nanomembrane Sensor for Detection of Nucleic Acids Using a Surface Charge Inversion Phenomenon. *Biosens Bioelectron* **2014**, *60*, 92–100. https://doi.org/10.1016/j.bios.2014.04.008.
- (28) Yin, Z.; Ramshani, Z.; Waggoner, J. J.; Pinsky, B. A.; Senapati, S.; Chang, H. C. A Non-Optical Multiplexed PCR Diagnostic Platform for Serotype-Specific Detection of Dengue Virus. *Sens Actuators B Chem* **2020**, *310*. https://doi.org/10.1016/j.snb.2020.127854.
- (29) Slouka, Z.; Senapati, S.; Shah, S.; Lawler, R.; Shi, Z.; Stack, M. S.; Chang, H. C. Integrated, DC Voltage-Driven Nucleic Acid Diagnostic Platform for Real Sample Analysis: Detection of Oral Cancer. *Talanta* **2015**, *145*, 35–42. https://doi.org/10.1016/j.talanta.2015.04.083.

- (30) Ramshani, Z.; Zhang, C.; Richards, K.; Chen, L.; Xu, G.; Stiles, B. L.; Hill, R.; Senapati, S.; Go, D. B.; Chang, H. C. Extracellular Vesicle MicroRNA Quantification from Plasma Using an Integrated Microfluidic Device. *Commun Biol* **2019**, *2* (1). https://doi.org/10.1038/s42003-019-0435-1.
- (31) Berzina, B.; Kim, S.; Peramune, U.; Saurabh, K.; Ganapathysubramanian, B.; Anand, R. K. Out-of-Plane Faradaic Ion Concentration Polarization: Stable Focusing of Charged Analytes at a Three-Dimensional Porous Electrode. *Lab Chip* 2022, 22 (3), 573–583. https://doi.org/10.1039/d1lc01011e.
- (32) Cagnin, S.; Caraballo, M.; Guiducci, C.; Martini, P.; Ross, M.; Santaana, M.; Danley, D.; West, T.; Lanfranchi, G. Overview of Electrochemical DNA Biosensors: New Approaches to Detect the Expression of Life. *Sensors* (*Switzerland*) **2009**, 3122–3148. https://doi.org/10.3390/s90403122.
- (33) Labib, M.; Sargent, E. H.; Kelley, S. O. Electrochemical Methods for the Analysis of Clinically Relevant Biomolecules. *Chem. Rev.* **2016**, 9001–9090. https://doi.org/10.1021/acs.chemrev.6b00220.
- (34) McDonald, J. C.; Whitesides, G. M. Poly(Dimethylsiloxane) as a Material for Fabricating Microfluidic Devices. *Acc Chem Res* **2002**, *35* (7), 491–499. https://doi.org/10.1021/ar010110q.
- (35) Xia, Y.; Whitesides, G. M. Soft Lithography. *Annu. Rev. Mater. Sci.* **1998**, 28 (1), 153–184. https://doi.org/10.1146/annurev.matsci.28.1.153.
- (36) Fishers, B. L. Streptavidin Coated Microspheres. *Prod. data sheet* **2004**, No. 721, 1–3.
- (37) Esteban Fernández De Ávila, B.; Watkins, H. M.; Pingarrón, J. M.; Plaxco, K. W.; Palleschi, G.; Ricci, F. Determinants of the Detection Limit and Specificity of Surface-Based Biosensors. *Anal Chem* **2013**, *85* (14), 6593–6597. https://doi.org/10.1021/ac4012123.
- (38) Kim, S.; Khanwale, M. A.; Anand, R. K.; Ganapathysubramanian, B. Computational framework for resolving boundary layers in electrochemical systems using weak imposition of Dirichlet boundary conditions, *Finite Elem Anal Des.* **2022**, *205*. https://doi.org/10.1016/j.finel.2022.103749.
- (39) Bazilevs, Y.; Calo, V. M.; Cottrell, J. A.; Hughes, T. J. R.; Reali, A.; Scovazzi, G. Variational Multiscale Residual-Based Turbulence Modeling for Large Eddy Simulation of Incompressible Flows. *Comput Methods Appl Mech Eng* **2007**, *197* (1–4), 173–201. https://doi.org/10.1016/j.cma.2007.07.016.
- (40) Saurabh, K.; Ishii, M.; Fernando, M.; Gao, B.; Tan, K.; Hsu, M. C.; Krishnamurthy, A.; Sundar, H.; Ganapathysubramanian, B. Scalable

- Adaptive PDE Solvers in Arbitrary Domains. In *International Conference for High Performance Computing, Networking, Storage and Analysis, SC*; IEEE Computer Society, 2021. https://doi.org/10.1145/3458817.3476220.
- (41) Druzgalski, C. L.; Andersen, M. B.; Mani, A. Direct Numerical Simulation of Electroconvective Instability and Hydrodynamic Chaos near an Ion-Selective Surface. *Physics of Fluids* **2013**, *25* (11). https://doi.org/10.1063/1.4818995.
- (42) Druzgalski, C. L.; Andersen, M. B.; Mani, A. Direct Numerical Simulation of Electroconvective Instability and Hydrodynamic Chaos near an Ion-Selective Surface. *Physics of Fluids* **2013**, *25* (11). https://doi.org/10.1063/1.4818995.

TOC Graphic

